MAX-PLANCK-INSTITUT FÜR PHYSIK

WERNER-HEISENBERG-INSTITUT

MPI-PhE/94-13
August 1994

Low-Energy X-Ray Detection in Cryogenic Detectors with Tungsten Thermometers

P. Colling, A. Nucciotti, C. Bucci,
S. Cooper, P. Ferger, M. Frank, U. Nagel, F. Pröbst, and W. Seidel

Max-Planck-Institut für Physik,
Föhringer Ring 6, D-80805 München, Germany

80805 München · Föhringer Ring 6

Low-Energy X-Ray Detection in Cryogenic Detectors with Tungsten Thermometers

P. Colling, A. Nucciotti*, C. Bucci,
S. Cooper, P. Ferger, M. Frank†, U. Nagel, F. Pröbst, and W. Seidel

Max-Planck-Institut für Physik,
Föhringer Ring 6, D-80805 Munich, Germany

Abstract

In the course of our development of calorimetric particle detectors with superconducting phase transition thermometers, we have succeeded in depositing epitaxial α-tungsten films on sapphire which have critical temperatures T_c near 15 mK. To our knowledge this is the first time that the T_c of bulk tungsten has been observed in thin films. Such films used as thermometers are very sensitive and provide good energy resolution: with 4 g and 32 g sapphire crystals energy resolutions of better than 100 eV (FWHM) for 1.5 keV x-rays have been achieved.

*Present address: Dip. di Fisica dell' Università di Milano, Milano, I-20133, Italy
†Present address: Lawrence Livermore National Laboratory, L-401, Livermore, CA 94550, USA.

1 Introduction

Massive cryogenic detectors are being developed as particle detectors with low energy threshold and good energy resolution for use in applications such as the search for hypothetical dark matter particles and the detection of neutrinoless double beta decay [1]. Compared to conventional detectors, a cryogenic calorimeter combines very good energy resolution, low energy threshold, flexibility in the choice of target nuclei, and good sensitivity to low-energy recoil nuclei, which have poor ionization efficiency [2].

A cryogenic calorimeter consists of an absorber crystal, in which the particle interaction takes place, and a thermometer which measures the resulting temperature rise. Operation in the millikelvin temperature range reduces thermal noise and takes advantage of the low heat capacities of materials at these temperatures.

The cryogenic calorimeters we are developing utilize dielectric absorber crystals, such as silicon or sapphire, and superconducting phase transition (SPT) thermometers [3, 4, 5, 6]. These thermometers profit from the rapid change in resistance of a superconductor in the narrow temperature region of its transition between the superconducting and normal phases. The temperature rise induced by deposited energies in the keV region is small enough that the thermometer remains well within its transition region. Since an SPT thermometers is only sensitive in its transition region, we need superconducting films with low transition temperatures T_c.

In this paper we report on the properties of tungsten films deposited on sapphire substrates in an ultra high vacuum system. We show that $T_c \sim 15\,\mathrm{mK}$ can be achieved [7, 8] and present first results using such films on 4 and 32 g sapphire crystals to detect low-energy x-rays.

2 Tungsten SPT Thermometers

2.1 Properties Of Tungsten

Tungsten is found in three different crystal structures, as reviewed in Ref. [9]. Two are found in both the bulk metal and in thin films: the b.c.c. structure known as α-W, which has lattice constant $a = 3.165\,\text{Å}$, and the A15 structure known as β-W, with $a \sim 5\,\text{Å}$. In thin films the f.c.c. structure of γ-W with $a \approx 4.2\,\text{Å}$ is also found.

The superconducting phase transition of bulk tungsten was first observed in 1964 by Gibson and Hein [10]. Later other groups confirmed the appearance of superconductivity in bulk tungsten, with T_c's between 12 and 17 mK [11, 12, 13, 14]. These measurements showed strong supercooling effects and a critical field of about 1 Gauss.

Soon after the observation of superconductivity in the bulk material, thin films of tungsten were found with much higher T_c's, ranging between 1 and 5 K. These measurements were made with equipment which could not reach temperatures below 1 K, so that a non-appearance of superconductivity could not be distinguished from $T_c \sim 15\,\mathrm{mK}$. Kammerer and Strongin [15] found the highest T_c's in films with the smallest grain size, with no superconductivity down to 0.9 K seen for films with grain size above 250 Å; annealing was found to reduce the T_c. Bond et al. [16] found the high T_c's to be associated with the formation of β-W; examination with an electron beam caused the films to convert to α-W and superconductivity could no longer be detected. Basavaiah and Pollack [17] found evidence that the β phase is

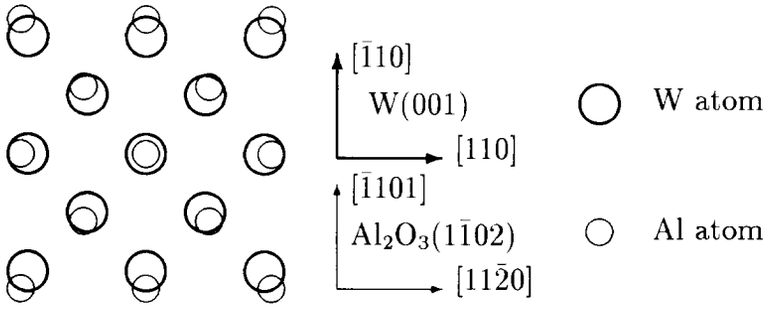

Figure 1: Epitaxial growth of (001) α-W on (1$\bar{1}$02) α-Al_2O_3.

stabilized by the presence of oxygen; films prepared by electron beam evaporation at 10^{-9} mbar showed only the α phase and no superconductivity down to 1 K. Chopra et al. [18] produced γ-W by sputtering in vacuum and found T_c's of 4–5 K; electron-beam evaporation onto a heated substrate gave only α-W, but the T_c was not measured. Later Schmidt et al. [19] found only α-W in films made by sputtering with noble gases; the films contained significant amounts of the gas atoms, had slightly expanded lattice sizes and T_c's of 3–5 K. Recently Irwin et al. [20] have used sputtering onto heated substrates and obtained T_c's near 90 mK.

From measurements on other superconductors [21] it is known that magnetic impurities in concentrations of a part per million (ppm) can reduce T_c's by 1 to 10 mK. For tungsten with its $T_c \sim 15$ mK this means that a few ppm could suppress superconductivity completely. Therefore extreme care must be taken during film preparation to avoid magnetic impurities.

Since we want to operate our detectors at low temperature, we need to produce α-W exclusively. Based on the evidence presented above, we decided to use electron beam evaporation onto heated substrates in a dedicated ultra high vacuum system.

2.2 Film Preparation And Deposition

We chose sapphire (α-Al_2O_3) as the absorber crystal due to its low specific heat capacity ($\Theta_{Debye} \approx 1040$ K, as calculated from its elastic constants) and its high melting temperature ($T_{melt} = 2310$ K) which avoids interdiffusion with the thermometer film. Also the presence of nuclear spin 5/2 in the ^{27}Al nuclei, which occur with 100% isotope frequency, is useful in testing for a possible spin-dependent interaction in a dark matter search. We used Czochralski-grown single crystals of sapphire[1] as the substrates for thermometer tests described in this section and as the absorber crystals for the detectors described in sect. 3.

To favor the growth of the b.c.c. lattice of α-W we have tried to achieve epitaxial growth. Epitaxial growth of α-W has been observed on selected planes of sapphire where the misfit is small [22]. For this reason we chose the (1$\bar{1}$02) plane or "r-plane" of sapphire. The expected epitaxial growth for α-W on this sapphire surface is with the W (001) plane parallel to the Al_2O_3 (1$\bar{1}$02) plane and the W [110] direction parallel to the Al_2O_3 [11$\bar{2}$0] direction (see fig. 1).

A tungsten single crystal[2] of 9 mm diameter was used as the evaporation material.

[1]The crystals were supplied by *Union Carbide* and *KCO*.

[2]The sample was supplied by *Johnson Matthey* with a nominal purity of 99.999%.

The residual resistivity ratio RRR of the crystal was measured using the decay of eddy currents [23] to be about 21 000. Its transition temperature $T_c \sim 16\,\mathrm{mK}$ was determined by placing it in a coil and measuring the change in the coil's self-inductance. The crystal was then cut into disks by spark erosion and etched in a $HF+HNO_3$ solution before being used for evaporation.

The films were prepared by electron-beam evaporation in a dedicated ultra high vacuum system equipped with a turbomolecular pump and a titanium sublimation pump. The sapphire crystal was laid in a tungsten holder which left most of the crystal surface exposed. (We avoided the use of a shadow mask, which could be a source of contamination or hinder attaining good vacuum near the crystal surface.) The crystal was heated by passing current through a tungsten sheet placed above the crystal. The substrate temperature T_{sub} was measured by an Rh/Pt thermocouple on the holder and could be controlled in a range between 200 and 1100 °C. The substrate heater and holder, which were heated to high temperatures during film deposition, were made out of non-magnetic materials. The substrate holder and the electron-beam evaporator were surrounded by liquid-nitrogen-cooled radiation shields. After a bake-out period of 24 h at 220 °C the system reached a base pressure of 6×10^{-12} mbar. During evaporation at a rate of 2 Å/s a pressure of 1×10^{-9} mbar could be maintained. With this system W films of thicknesses between 2400 and 6000 Å were deposited on test substrates with T_{sub} ranging from 200 to 1100 °C.

2.3 Crystal Structure

The crystal structure of the films were analyzed using a Bragg-Brentano x-ray diffractometer with a wavelength of 1.54 Å. In θ-2θ scans the incident x-ray beam and the detected, reflected beam are both at angles θ relative to the plane of the substrate, and only reflections from crystal planes parallel to the substrate surface can be seen. In all the tungsten films only the b.c.c. structure was detected with a mean lattice constant of 3.167±0.002 Å. No evidence was found for the presence of β or γ-W. For $T_{sub} \geq 500\,^{\circ}\mathrm{C}$ the expected epitaxial growth (001) W $\parallel$ $(1\bar{1}02)$ Al_2O_3 was observed: only the reflection at the angle expected for the (002) reflection from the (001) plane of α-W was detected (fig. 2 a). To confirm epitaxy and check the relationship of the directions in the substrate plane, a φ-scan on the {202} planes of α-W around an axis perpendicular to the substrate surface was performed (fig. 2 b). Only the four reflections of the {202} planes were detected. The [100] direction of tungsten is rotated by 45 degrees with respect to the $[11\bar{2}0]$ direction of sapphire, as expected.

With increasing T_{sub} the crystalline structure of the films improved. This was seen in the increasing sharpness of the (002) α-W reflection peak in the θ-2θ scans as well as the tendency of the residual resistivity ratio to increase with higher substrate temperatures.

2.4 Superconductivity

For superconductivity measurements each substrate was mounted in a copper holder that was screwed directly onto the mixing chamber of the $^3He/^4He$ dilution refrigerator described in sect. 3.1.1. The holder temperature was measured with a calibrated carbon resistor. The holder could be cooled to below 9 mK. The thermal contact between the holder and the film was provided by a spring-loaded gold tip. Electrical

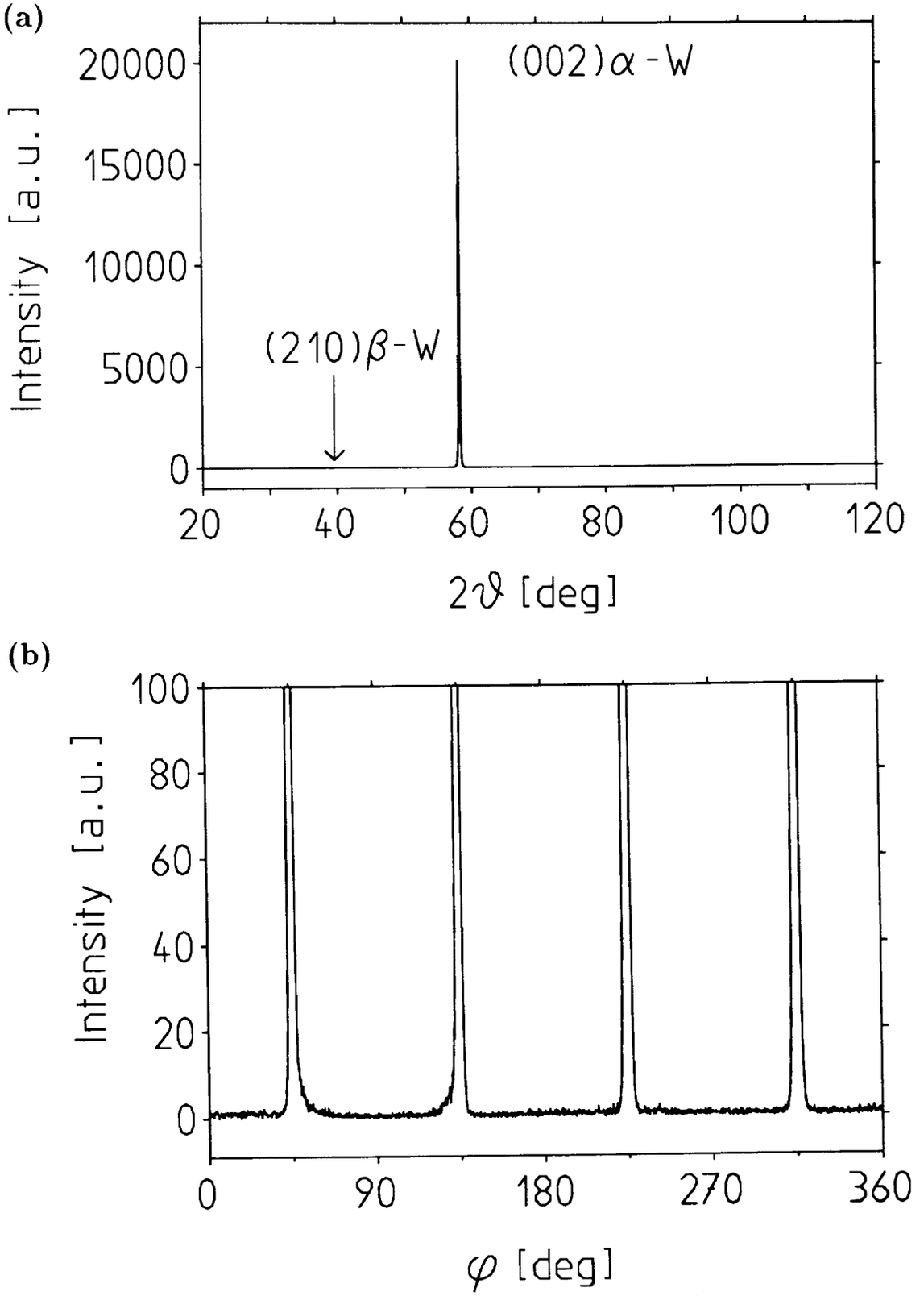

Figure 2: (a) θ-2θ scan of a tungsten film of thickness 2500 Å deposited on a test substrate at $T_{sub} = 500\,^{\circ}\mathrm{C}$. Only the (002) reflection of α-W at $2\theta = 58$ degrees is observed. The expected position of the strongest β-W reflection is indicated. (b) φ scan on {202} planes of same film. $\varphi = 0$ degrees corresponds to the $[11\bar{2}0]$ direction of the sapphire substrate. The four reflections are due to the {202} planes of α-W.

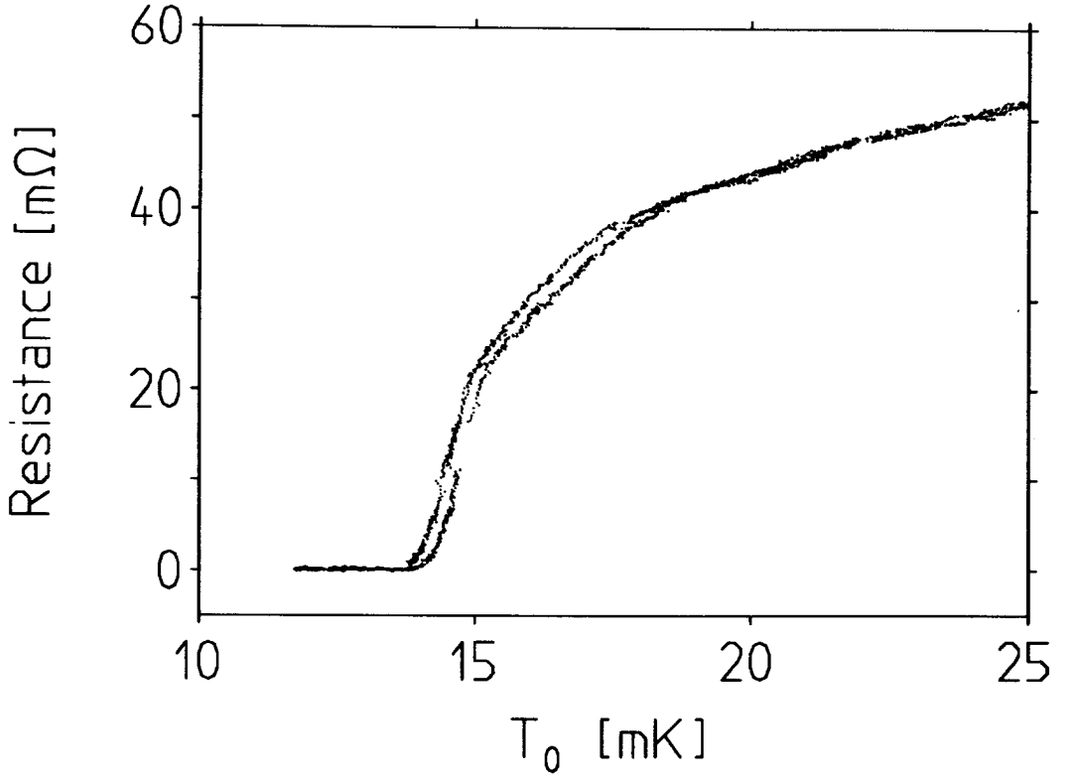

Figure 3: Superconducting transition of film from fig. 2 measured with $I_{rms} = 4\,\mu$A. T_0 is the holder temperature. The left curve is measured while cooling down, the right one while warming up. The slight hysteresis depended on the rate of temperature change, and was presumably due to the time constant of the carbon thermometer.

contact to the film was provided by indium press contacts and the film's resistance was measured with a lock-in amplifier using a four-point AC readout. The resistance was recorded while sweeping the temperature through the region of the transition. The superconducting transition of the film of fig. 2 is shown in fig. 3. To our knowledge this is the first tungsten film with a measured superconducting transition near 15 mK.

Films deposited at $T_{sub} > 700\,^{\circ}$C had transitions at lower temperatures or showed no superconductivity at all down to the lowest temperatures reached (< 9 mK). Analyses performed on these films using secondary-ion mass spectrometry (SIMS) detected contaminations of Fe, Cr, and Ni concentrated at the substrate-film interface. We believe that these magnetic impurities came from inside the evaporation system and were increasingly released when higher temperatures were used during preparation of the films.

3 Detectors With Tungsten SPT Thermometers

In this section we present results obtained with our first two detectors using tungsten thermometers. The experimental setup is similar to that described in in ref. [4]. Here details of the mechanical setup, the readout circuit, and the x-ray source which are specific to the detectors described in this paper are given. Then we describe the 4 g and 32 g detectors in turn.

3.1 Experimental Setup

3.1.1 Dilution Refrigerator

For the work described in this paper we built a new dilution refrigerator with a base temperature of about 8 mK. Special care was put into the vibrational isolation, placing the pumps outside the building and passing the pumping lines through sand-filled boxes before they reach the refrigerator. A double-gimbal configuration [24] at the top of the refrigerator further isolates the ^{3}He pumping line. The refrigerator is supported by a massive wooden top plate which rests on air dampers and is loaded with lead bricks to lower the resonance frequency.

To reduce electromagnetic interference, the refrigerator together with the sensitive electronics are enclosed in a Faraday cage. The experimental volume inside the refrigerator is surrounded by a Cryoperm[3] magnetic shield and an Al can which acts as a superconducting shield against electromagnetic interference.

3.1.2 Detector Assembly

The parameters of the two detectors discussed in this paper are summarized in table 1. For each detector the absorber was a single crystal of sapphire. The tungsten SPT thermometer was deposited onto a $(1\bar{1}02)$ surface of the crystal. During the deposition the crystals were heated to 500 °C. The shape of the thermometer was defined after deposition to $5 \times 3\,\mathrm{mm}^2$ by photolithography and wet chemical etching using a solution of H_2O+$K_3Fe(CN)_6$+$C_2H_8N_2$+HCl with a pH value of 8 [25]. Gold contact pads ($3 \times 0.3\,\mathrm{mm}^2$) were ion-beam sputtered onto each end of the thermometer after cleaning the tungsten surface in the ion beam. The shape of the contact pads was defined with a photolithographic lift-off technique. Electrical and thermal contact to the thermometer was made by ultrasonic wedge bonding of Al and Au wires, respectively, to these contact pads.

Each detector was placed in a massive copper housing which served as a constant temperature bath. The detector rested in the housing on three screw-adjustable tips; the 4 g detector was additionally held from the top by two spring-loaded tips, the 32 g detector by two tips on one side and a spring-loaded tip on the other. Each tip ended in a small sapphire ball, which had only a small contact area with the detector crystal, providing good thermal isolation of the detector from the copper housing. A sketch of the assembly for the 32 g detector is shown in fig. 4.

Thermal contact between the housing and the detector was made by gold wires bonded to one of the two contact pads and to the copper housing. Electrical contact between the thermometer and the external circuit of fig. 5 was provided by aluminum wires bonded to the contact pads of the thermometer and to isolated pads on the copper housing; during calorimeter operation these wires were superconducting and had negligible thermal conductance.

The thermodynamic properties of each detector at 15 mK are given in table 1. The heat capacity C_a of the sapphire was calculated using $\Theta_D = 1040\,\mathrm{K}$ and $C_a = 234\,N\,k_B(T/\Theta_D)^3\,\mathrm{J{\cdot}K^{-1}}$, where N is the number of atoms in the crystal. The heat capacity of the thermometer was roughly estimated from the electronic heat capacity of tungsten in its normal state using $C_e = n_{moles}\,\gamma\,T$ with $\gamma = 1.0{\times}10^{-3}$ $\mathrm{J{\cdot}mol^{-1}K^{-2}}$ [13]. The contact pads contributed less than 1 % to the thermometer

[3]Cryoperm is a magnetic shielding material which functions at cryogenic temperatures. Cryoperm is a registered trademark of Vacuumschmelze GmbH, Hanau, Germany.

Table 1: Parameters of the 4 g and 32 g detectors at T = 15 mK.

Detector:	**4 g**	**32 g**
Absorber:		
Material	sapphire	sapphire
Size	$20 \times 10 \times 5\,\mathrm{mm}^3$	$40 \times 20 \times 10\,\mathrm{mm}^3$
$(1\bar{1}02)$ surface	$20 \times 10\,\mathrm{mm}^2$	$40 \times 20\,\mathrm{mm}^2$
Heat capacity C_a	1.1 pJ/K	9.1 pJ/K
Thermometer:		
Tungsten film	$3 \times 5\,\mathrm{mm}^2 \times 250\,\mathrm{nm}$	$3 \times 5\,\mathrm{mm}^2 \times 280\,\mathrm{nm}$
Gold contact pads	$3 \times 0.3\,\mathrm{mm}^2 \times 400\,\mathrm{nm}$	$3 \times 0.3\,\mathrm{mm}^2 \times 400\,\mathrm{nm}$
T_c (low current limit)	14 mK	15 mK
R_{th} (n.c.)	95 mΩ	55 mΩ
RRR	3	5
C_e (n.c.)	6.7 pJ/K	7.5 pJ/K
Thermal Coupling:		
Material	2 gold wires	1 gold wire
wire diameter, length	25 μm, 7 mm	25 μm, 15 mm
total conductance G_{Au}	20 nW/K	8 nW/K

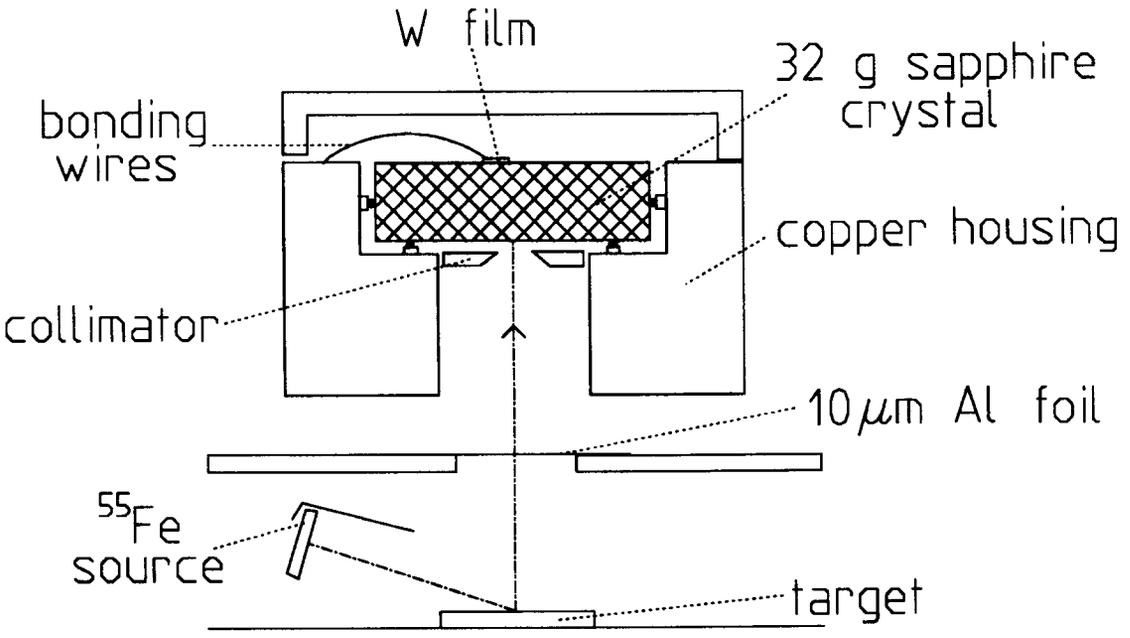

Figure 4: Schematic of the 32 g detector assembly.

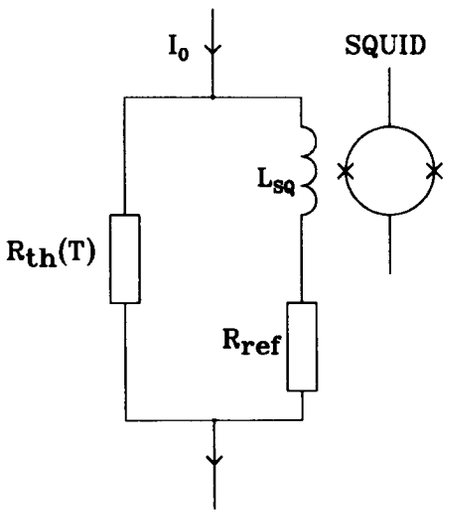

Figure 5: Schematic of the readout circuit. $R_{th}(T)$ is the tungsten thermometer resistance (the normal-conducting values are given in table 1); $R_{ref} = 50\,\mathrm{m}\Omega$ is a constant reference resistor; $L_{SQ} = 1.3\,\mu\mathrm{H}$ is the SQUID coupling inductor. I_0 is the constant drive current. A change of $R_{th}(T)$ affects the branching of the current, which is detected by the SQUID.

heat capacity. The thermal conductance G_{Au} of the gold wires was calculated from their electrical resistance at 4 K using the Wiedemann-Franz law (wires of different purity were used for the two detectors).

The copper housing was mechanically attached to the mixing chamber of the dilution refrigerator but thermally isolated with Vespel[4] spacers. The thermal connection between the housing and the mixing chamber was provided by a copper wire chosen to give a thermal time constant of roughly 20 seconds. A calibrated NTD-Ge thermometer and a resistive heater were used to stabilize the temperature of the housing. In this configuration the housing acts as a constant temperature bath for the detector. To avoid long time constants in the housing temperature, the use of non-crystalline materials (glues, plastics, etc.) was limited and magnetic materials were avoided (the springs were made of tungsten). The housing was made of OFHC[5] copper and annealed in vacuum at about 1000 °C for more than two days to increase its thermal conductivity and remove hydrogen inclusions [26].

3.1.3 Electrical Readout

The low electrical resistance of SPT thermometers is well suited to measurement with a dc-SQUID[6]. A constant drive current I_0 was fed into the readout circuit of fig. 5 which consisted of two parallel branches: one with the thermometer $R_{th}(T)$ and the other with a reference resistor R_{ref} in series with the coupling inductor L_{SQ} of the SQUID. When a particle deposits energy in the sapphire crystal, the temperature and thus the resistance of the thermometer rises, so that a larger current I_{SQ} flows

[4]Vespel is a registered trademark of Dupont.

[5]Oxygen Free High Conductivity

[6]We used a Model 581 SQUID from 2G Enterprises.

through the SQUID coupling inductor:

$$I_{SQ} = I_0 \frac{R_{th}}{R_{th} + R_{ref}} . \quad (1)$$

For changes slow compared to the L-R time constant of the circuit (ca. 20 μs), a small resistance change dR_{th} leads in first order to a change

$$dI_{SQ} \approx I_0 \frac{R_{ref}}{(R_{th} + R_{ref})^2} dR_{th} . \quad (2)$$

The operating point of the detector is defined by the drive current I_0 and by the temperature T_0 of the housing. The temperature of the detector is higher than that of the housing due to resistive heating in the thermometer. The choice of operating point is a compromise between the need of using a high readout current, the heating of the detector, the local steepness of the transition, and the current dependence of the transition steepness and of the noise.

The current I_0 was supplied by a floating battery-powered current source. The current leads were rf-filtered inside the cryostat. The readout circuit was electrically grounded only by the thermal connection of the thermometer to the copper housing. The reference resistor R_{ref} was mounted in a closed copper box attached to the mixing chamber. The SQUID itself and its coupling inductor L_{SQ} were inside a Nb tube in the liquid helium. Twisted pairs of Nb-Ti wires were used for the parallel circuit. Nb and Pb-Sn tubes shielded the wires going to the SQUID and to the detector, respectively. The SQUID electronics, the current source, and the devices for temperature stabilization were placed inside the Faraday cage.

The output voltage signal of the SQUID electronics exited the Faraday cage through 50 kHz low-pass filters and was then split, with one branch ac-coupled to a trigger unit and the other passing through an anti-aliasing filter and then dc-coupled to a 12-bit transient recorder. The time base of the transient recorder was chosen to provide about 10 bins in the rise of the pulse and the record length was chosen long enough to cover most of the pulse's decay. The cutoff frequency of the filter was set to less than half of the transient recorder sampling rate. Online software cuts rejected events that exceeded the range of the transient recorder.

3.1.4 Low Energy X-Ray Source

To test the energy response of the detectors at different energies we used fluorescence x-rays between 1.5 and 6 keV. The primary source was ^{55}Fe, which provided the 6 keV x-rays of Mn. An Al/V composite target (for the 4 g detector) or an Al/Ti composite target (for the 32 g detector) was exposed to the primary x-rays. The fluorescence x-rays of the target materials and the Rayleigh-scattered Mn x-rays could be observed; their energies are given in table 2. A 10 μm Al foil prevented Auger and photoelectrons from reaching the detector. The geometry was chosen to prevent the primary x-rays from being seen directly by the detector or from hitting the Al foil (see fig. 4). A roughly equal intensity of the K_α lines was achieved by proper choice of the relative areas of the target elements. The x-ray rate was reduced to a few Hz by a collimator of a few mm diameter built into the detector housing. The x-rays struck the face of the crystal opposite to the thermometer.

Table 2: Energies of detectable x-rays.

	E_{K_α} [keV]	E_{K_β} [keV]
Al	1.487	-
Ti	4.509	4.932
V	4.950	5.426
Mn	5.895	6.490

3.2 4 g Sapphire Detector

The parameters of the 4 g detector are summarized in table 1. The x-ray fluorescence source with the Al/V composite target illuminated a 1.3 mm diameter spot on the crystal. Data were acquired at several operating points. Offline software cuts were applied to discard pulses which were degraded by pile-up or which exceeded the dynamic range of the electronics or the slew rate of the SQUID.

The recorded temperature pulses showed an exponential rise time τ_{rise} and two exponential decay times τ_{fast} and τ_{slow} (fig. 6). The pulse shape could be described by

$$A(t) = -A_{tot}\, e^{-\frac{(t-t_0)}{\tau_{rise}}} + A_{fast}\, e^{-\frac{(t-t_0)}{\tau_{fast}}} + A_{slow}\, e^{-\frac{(t-t_0)}{\tau_{slow}}} + B \qquad (3)$$

for $t \geq t_0$, and $A(t) = B$ for $t < t_0$. Here B is the baseline, t_0 is the pulse onset, and $A_{tot} \equiv A_{fast} + A_{slow}$ assures continuity at $t = t_0$. Each pulse was fit with the function A(t) with A_{fast}, A_{slow}, B, t_0, τ_{rise}, τ_{fast}, and τ_{slow} as free parameters. The amplitudes A were converted from transient recorder units into temperature units using the slope of the transition at the chosen operating point. Table 3 shows the parameter values obtained at two different operating points.

The data used for the energy spectrum of fig. 7 were recorded with a readout current of $I_0 = 25\,\mu$A. The holder temperature was stabilized at 9 mK and was constant to 2.5 μK FWHM, as measured by the SQUID baseline. The transient recorder was set to 10 μs per channel and 4096 channels per event. The pulse-height spectrum was obtained after smoothing each pulse with a 50-channel moving average. The energy calibration was then determined by fitting the K_α peak positions with a straight line passing through the origin. With this linear calibration the positions of the K_α peaks agree with the expected ones within 0.5 %. Use of the approximation of eq. (2) causes about half of this small non-linearity.

Fitting the peaks in the spectrum of fig. 7 with Gaussian curves yields FWHM energy resolutions of 78±1 eV at 1.5 keV, 170±2 eV at 5 keV, and 207±3 eV at 6 keV (the K_α lines of Al, V, and Mn, respectively). The baseline width was measured after performing the 50 channel average by comparing one point in the pre-trigger range (the first 10 ms in fig. 6) to the average of all the pre-trigger points in the same event. The resulting FWHM baseline width was about 56 eV, which corresponds to a temperature resolution of roughly 0.4 μK. The energy dependence of the resolution can be parameterized as the sum in quadrature of a constant term for the electronic noise and an excess term. The cause of this excess term is not yet understood. It shows a roughly linear dependence on the energy. Making a cut requiring the SQUID baseline position to be within ±1 μK of the desired operating point improves the resolution only by a few eV, showing that shifts of the operating point are not a significant contribution to the peak width. Measurements on other detectors of this

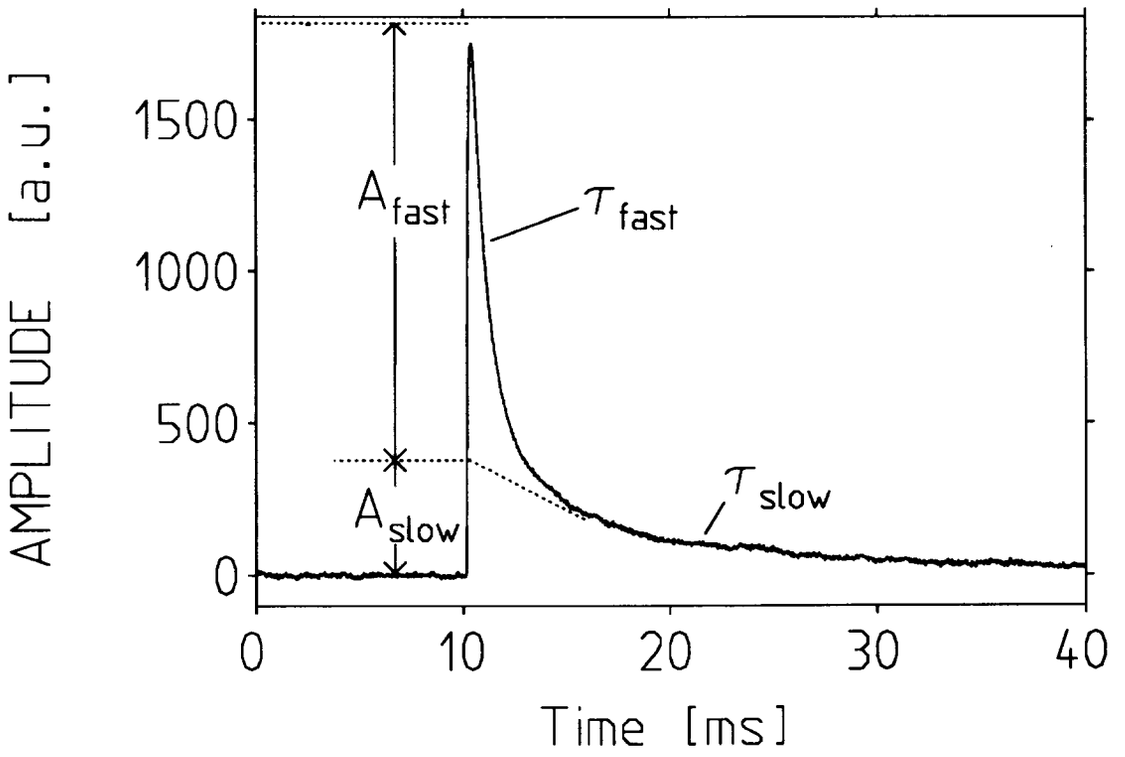

Figure 6: A typical pulse resulting from the absorption of a 6 keV x-ray. The pulse shape parameters are illustrated. The operating point for this pulse is $T_0 = 9\,\mathrm{mK}$ and $I_0 = 25\,\mu\mathrm{A}$.

Table 3: Fitted values of the pulse shape parameters for Mn K_α pulses at different positions r in the transition, where $r \equiv (R_{th}(T) - R_{th}^{sc})/(R_{th}^{nc} - R_{th}^{sc})$, $R_{th}(T)$ is the resistance at each operating point, R_{th}^{sc} is its superconducting value, and R_{th}^{nc} its normal-conducting value. R_{th}^{sc} was 21 mΩ and 9 mΩ for the 4 g and 32 g detectors, respectively; these values were measured where the transition leveled off at low temperature, and were apparently due to contact resistances in the circuit. The R_{th}^{nc} values were 96 mΩ and 55 mΩ, respectively. For the 4 g detector the readout current was $I_0 = 3\,\mu\mathrm{A}$; for the 32 g detector $I_0 = 10\,\mu\mathrm{A}$. The errors given for the fit parameters are the rms widths of the distributions combined with an estimate of the error in the slope of the transition curve used to convert the SQUID signal to μK.

Detector	r	A_{fast} [μK]	A_{slow} [μK]	τ_{rise} [ms]	τ_{fast} [ms]	τ_{slow} [ms]
4 g	0.05	31 ± 5	8 ± 2	0.06 ± 0.01	0.8 ± 0.1	13 ± 2
	0.23	37 ± 5	8 ± 3	0.06 ± 0.01	0.8 ± 0.1	12 ± 4
32 g	0.17	4 ± 1	3 ± 1	0.66 ± 0.06	2.6 ± 0.4	27 ± 4
	0.40	8 ± 2	5 ± 1	0.34 ± 0.04	2.4 ± 0.5	25 ± 6
	0.79	34 ± 6	11 ± 4	0.27 ± 0.02	1.7 ± 0.2	16 ± 3

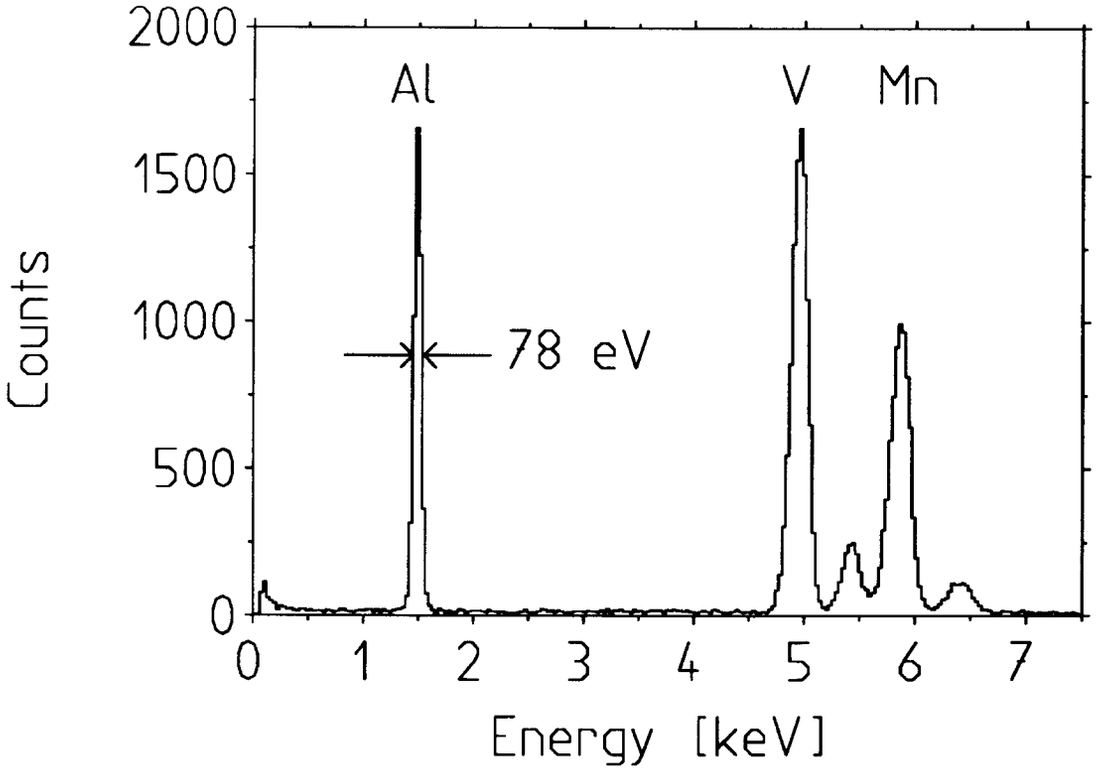

Figure 7: Energy spectrum recorded with the 4 g crystal when irradiated with the Al/V x-ray fluorescence source.

type [4, 5] have shown that position dependence is unlikely to explain the excess peak width.

The application of an optimal filter [27] improves the resolution at the low-energy end of the spectrum, where the contribution of the electronic noise is more important. Optimal filtering together with the cut on the baseline position gives a FWHM baseline width of 49 eV and a FWHM energy resolution of 60 ± 1 eV at 1.5 keV.

The use of a higher readout current does not correspondingly increase the signal-to-noise ratio because the observed noise increases with the current. To study the electronic noise we recorded a few thousand randomly-triggered baselines at different operating points. Events with obvious pulses or tilted baselines were rejected. The spectral density of the current noise was calculated using a fast Fourier transform. Fig. 8 shows the result for various readout currents in the same position ($R_{th} = 41\,\mathrm{m}\Omega$) on the transition where the data of fig. 7 were taken. For zero readout current the noise spectrum is flat at a level of about $6 \times 10^{-24}\,\mathrm{A^2/Hz}$. This agrees with the expected noise of the readout circuit, which is dominated by the Johnson noise (4kT/R) of the thermometer and the reference resistances. The SQUID noise of $4 \times 10^{-25}\,\mathrm{A^2/Hz}$ is negligible. As the readout current is increased an additional noise contribution appears as shown in fig. 8. The cause of this current-dependent noise is not yet understood. It is not present outside the transition region of the thermometer.

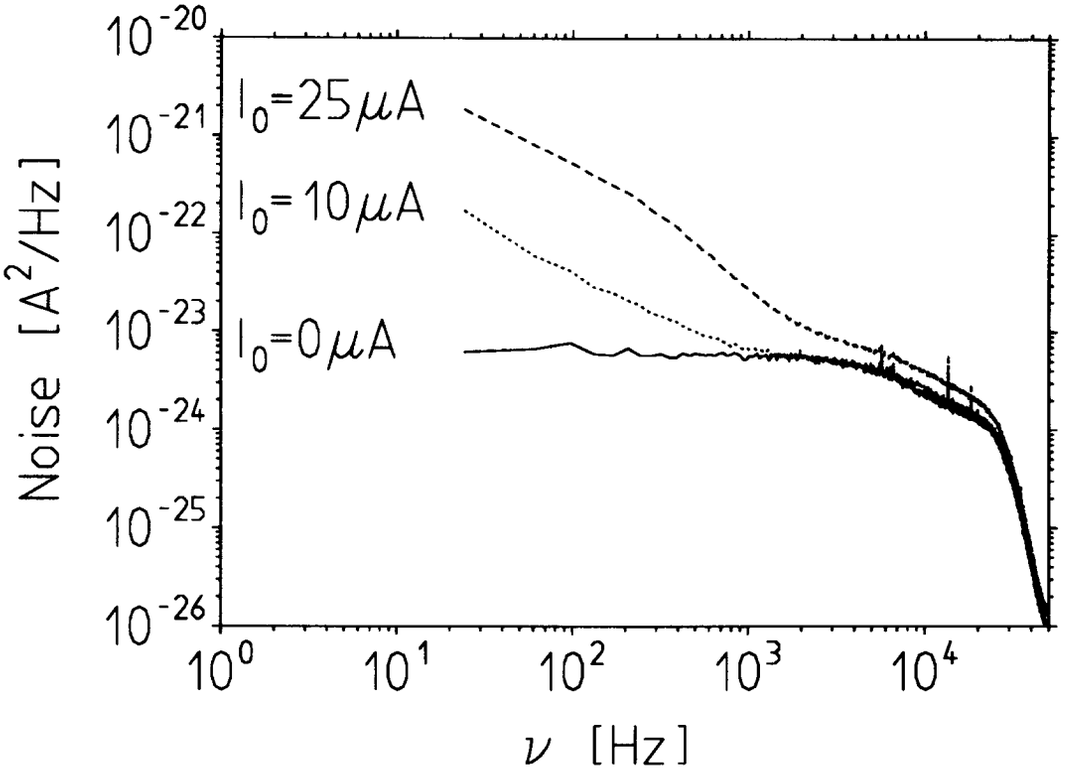

Figure 8: Spectral density of the current noise at the SQUID input coil for the 4 g detector. It is plotted for positive frequencies ν (multiplied by 2 to account for the negative frequencies not shown) for $R_{th} = 41\,\mathrm{m}\Omega$ and various readout currents. (The operating temperature was adjusted to obtain the same R_{th} for each readout current.)

3.3 32 g Sapphire Detector

For the 32 g detector (see table 1) the thermometer size is the same as that for the 4 g detector. The thermometer transition was first measured with the magnetic shield installed, as for the 4 g detector. To test its effect, the shield was then removed. A smoothening of the transition curve accompanied by a shift of 2 mK towards lower temperatures was observed. The data described below were taken without the magnetic shield.

The presence of a high rate of background pulses in this detector made it difficult to measure the transition. A large pulse can cause the SQUID to lose flux lock, resulting in a sudden offset in the measured transition curve. Such offsets can be avoided by using not a constant readout current I_0 but a square-wave of $\pm I_0$, which causes the same heating and current effects in the thermometer as a constant I_0. The rise time of the square wave was chosen slow enough to avoid flux loss. The change ΔV_{SQ} in the SQUID signal for each change in sign of the square wave then corresponds to twice the thermometer resistance. Many such points were taken while slowly changing the temperature of the holder. Pulses were removed from the resulting data by keeping only the lowest ΔV_{SQ} of each successive 10 data points. The remaining ΔV_{SQ} values were then converted into R_{th} to get the transition shown in fig. 9 a.

To obtain an energy spectrum the fluorescence x-ray source with the Al/Ti com-

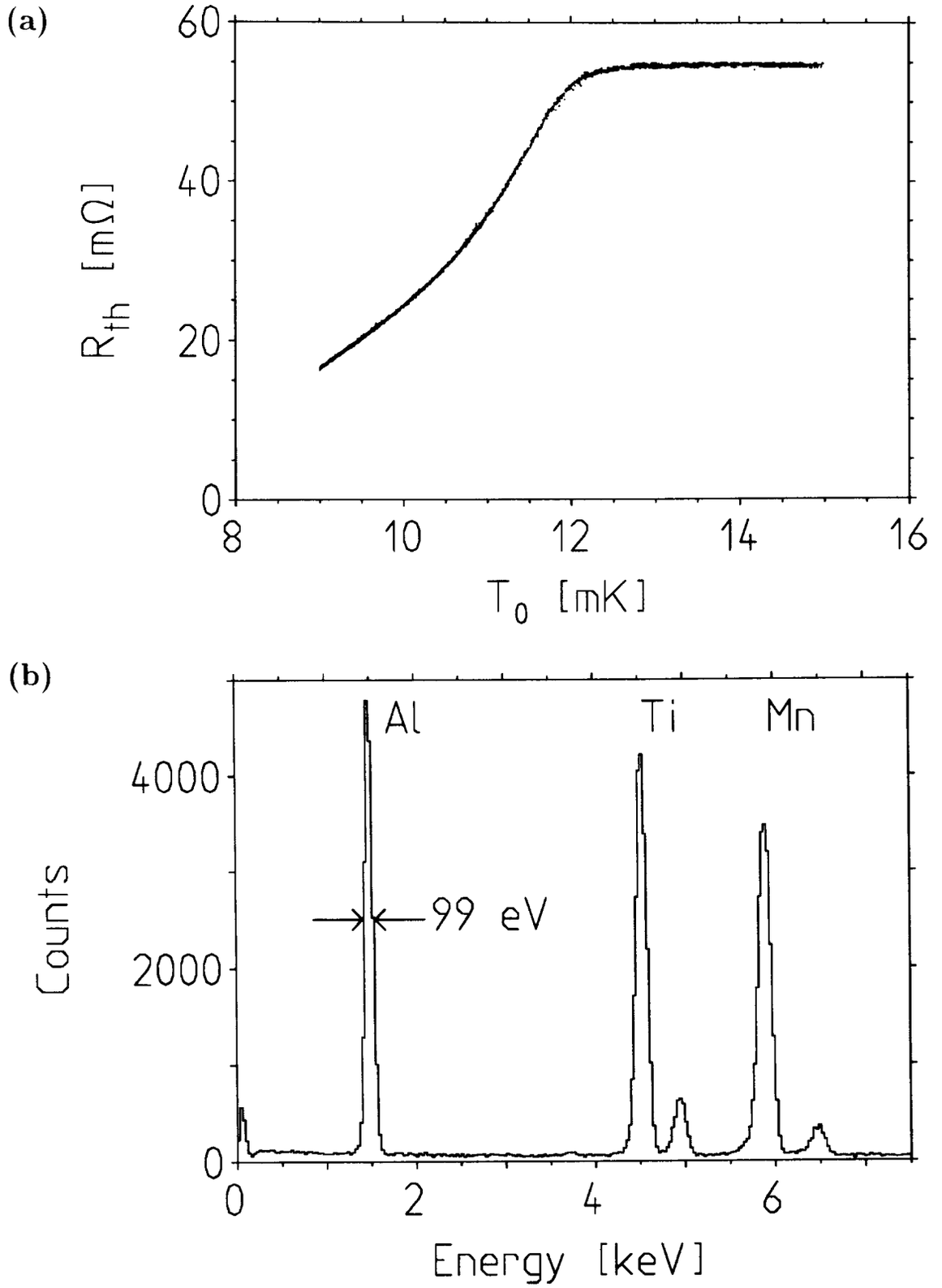

Figure 9: (a) Superconducting transition of the tungsten thermometer on the 32 g crystal measured with $I_0 = 15\,\mu$A and magnetic shield removed. (b) Pulse height spectrum measured while irradiating the detector with the Al/Ti fluorescence x-ray source. The operating point was $T_0 = 12$ mK and $I_0 = 15\,\mu$A, corresponding to $r = 0.79$ in table 3.

posite target was used to illuminate a 3.6 mm diameter spot on the detector. The total event rate was about 10 Hz. A sample of 140 000 events was obtained in a 30 h run with the holder temperature stabilized at 12 mK and using a readout current I_0 of 15 μA. The transient recorder was set to 10 μs per channel. Due to the high background rate, offline cuts were needed to reject events with pile-up or which were triggered by SQUID resets. The latter were eliminated by calculating the average rise time of all pulses and rejecting pulses which had rise times shorter than 1/2 the average value. Some pile-ups were eliminated by rejecting pulses with rise times longer than twice the average value. Remaining pile-ups were reduced by fitting the baseline in the pre-trigger region with a straight line, and rejecting events if χ^2/d.o.f.> 4 for the fit or if the tilt of the baseline was more than 100 eV/ms. The final sample contained 86 000 events.

The pulse height was determined after smoothing each pulse with a moving 50 channel average. The resulting spectrum is shown in fig. 9 b. The energy scale was set by fitting the positions of the three K_α lines with a straight line passing through zero. The energy linearity of the detector response was better than 0.3 %. Fitting Gaussian curves to the K_α lines in fig. 9 b gave an FWHM energy resolution of 99 $\pm$ 1 eV at 1.5 keV, 137 $\pm$ 1 eV at 4.5 keV, and 161 $\pm$ 2 eV at 6 keV (the Al, Ti,and Mn K_α lines, respectively). Since the baseline for this detector often had a significant slope due to pile-up, the baseline width was measured after performing the 50 channel average by fitting a straight line to the points in the pre-trigger range and taking its distance to a single point in the pre-trigger. The resulting baseline width was about 32 eV FWHM. A study of the energy dependence of the excess broadening was more difficult than for the 4 g detector because of the high background rate. As for the 4 g detector there was some evidence of a current-dependent excess noise in the transition.

The pulses were fit with eq. (3), as for the 4 g detector. Here the pulse shape parameters were found to depend on the operating point in the transition. As R_{th} increases the amplitudes increase and the time constants decrease (table 3). These effects are not yet understood. They preclude making any simple deduction on the dependence of the signal on the crystal size.

Based on our model for detectors of this type [6], our previous detectors operated in the "bolometric mode", where the fast amplitude is controlled by the thermal coupling of the thermometer and the fast decay time is given by the absorption of the non-thermal phonons. Due to their lower operating temperature, we expect both the 4 and 32 g detectors described here to operate in the as-yet untested "calorimetric mode", where the rise time is given by the absorption of the non-thermal phonons and the fast amplitude is controlled by the heat capacity of the thermometer. The model for this mode needs further development before a comparison to the data can be made.

4 Conclusions

We have succeeded in producing α-tungsten films with superconducting phase transitions near the $T_c \sim 15$ mK of bulk tungsten. With such a thermometer on a 32 g sapphire single crystal an energy resolution of 99 eV (FWHM) for 1.5 keV x-rays has been achieved. To our knowledge this is the best reported resolution per unit detector mass for a cryogenic detector. The good energy resolution at low deposited

energies and the low threshold of the detector are promising for further development as a prototype detector for our planned experiment searching for dark matter particles [28].

5 Acknowledgements

We thank our colleagues at the Technical University of Munich for their collaboration and for providing space for our evaporation system, and especially E. Kellner for his technical support. The x-ray diffraction analysis was performed by G. Neff. The photolithographic masks were made by H. Böving. We thank A. Rulofs and the workshop of our institute for their support, especially for their excellent work in building the dilution refrigerator. The temperature control of the sample holder in the refrigerator was performed using an NTD-Ge thermistor supplied by E. Haller, and other thermometers were supplied by K. Neumaier.

References

[1] Proc. Fifth Int. Workshop on Low Temperature Detectors, July 29 – Aug. 3, 1993, Berkeley, California, USA, eds. S.E. Labov and B.A. Young, J. Low Temp. Phys. Vol. 93 Nr. 3/4 (1993).

[2] J. Lindhard, V. Nielsen, M. Scharff, and P. Thomsen, Mat. Fys. Medd. Dan. Vid. Selsk. 33 (1963) 10.

[3] W. Seidel, G. Forster, et al., Phys. Lett. B 236 (1990) 483.

[4] M. Frank, D. Dummer, et al., Nucl. Instr. and Meth. A 345 (1994) 367; M. Frank, PhD thesis (in German), Technische Universität München (1993), MPI preprint MPI-PhE/93-16.

[5] P. Ferger et al., Phys. Lett. B 323 (1994) 95.

[6] F. Pröbst et al., MPI preprint MPI-PhE/94-14 (1994), to be sub. to Nucl. Inst. and Meth.; M. Frank et al. in ref. [1], p. 213; F. Pröbst, Proc. Seventh Int. Conf. on Phonon Scattering in Condensed Matter, Aug. 3–7, 1992, Ithaca, New York (Springer-Verlag, Berlin, 1993), p. 477.

[7] P. Colling, Diplom thesis (in German), Technische Universität München, MPI preprint MPI-PhE/92-10 (1992).

[8] W. Seidel, Proc. 12th Int. Vac. Congress, The Hague, Oct. 1992, eds. A.W. Klein, S. Hofmann, and A. Rockett, pub. in Thin Solid Films 228 (1993) 186.

[9] M. Gasgnier, L. Nevot, P. Baillif, and J. Bardolle, Phys. Stat. Sol. (a) 79 (1983) 531.

[10] J. W. Gibson and R. A. Hein, Phys. Rev. Lett. 12 (1964) 688.

[11] R. T. Johnson, O. E. Vilches, and J. C. Wheatley, Phys. Rev. Lett. 16 (1966) 101.

[12] W. C. Black, R. T. Johnson, and J.C. Wheatley, J. Low Temp. Phys. 1 (1969) 641.

[13] B. B. Triplett et al., J. Low Temp. Phys. 12 (1973) 499.

[14] R. J. Soulen, Jr. and R. B. Dove, NBS Special Publication 260-62, "SRM 768: Temperature reference standard for use below 0.5 K", (National Bureau of Standards, Washington, 1979).

[15] O.F. Kammerer and M. Strongin, Phys. Lett. 17 (1965) 224, and Proc. Int. Symp. on Basic Problems in Thin Film Physics, Clausthal-Göttingen, Sept. 1965, eds. R. Niedermayer and H. Mayer, (Vandenhoeck & Ruprecht, Göttingen, 1966) p. 511; J.E. Crow, M. Strongin, R.S. Thompson, and O.F. Kammerer, Phys. Lett. 30A (1969) 161.

[16] W.L. Bond, A.S. Cooper, K. Andres, G.W. Hull, T.H. Geballe, and B.T. Mattias, Phys. Rev. Lett. 15 (1965) 260.

[17] S. Basavaiah and S.R. Pollack, Appl. Phys. Lett. 12 (1968) 259 and J. Appl. Phys. 39 (1968) 5548. See also N.N. Konokova, É.M. Reĭkhrudel', and G.V. Smirnitskaya, Sov. Phys. Tech. Phys. 27 (1982) 60.

[18] K.L. Chopra, Phys. Lett. 25A (1967) 451; K.L. Chopra, M.R. Randlett, and R.H. Duff, Appl. Phys. Lett. 9 (1966) 402 and Phil. Mag., July 1967, p. 261.

[19] P.H. Schmidt, R.N. Castellano, H. Barz, A.S. Cooper, and E.G. Spencer, J. Appl. Phys. 44 (1973) 1833; P.H. Schmidt, J. Vac. Sci. Tech. 10 (1973) 611.

[20] K.D. Irwin, B. Cabrera, B. Tigner, and S. Sethuraman, Proc. IV Int. Workshop on Low Temperature Detectors for Neutrinos and Dark Matter, Oxford, Sept. 1991, ed. N.E. Booth and G.L. Salmon (Editions Frontières, Gif-sur-Yvette, 1992), p. 209.

[21] G. Boate, G. Gallinaro, and C. Rizzuto, Phys. Rev. 148 (1966) 353.

[22] A. Miller, H. M. Manasevit, D. H. Forbes, and I. B. Cadoff, J. Appl. Phys. 37 (1966) 2921; J.H. Souk, A. Segmüller, and J. Angilello, J. Appl. Phys. 62 (1987) 509.

[23] C.P. Bean, R.W. Boates, and L.B. Nesbitt, J. Appl. Phys. 30 (1959) 1976.

[24] W. P. Kirk, M. Twerdochlib, Rev. Sci. Instrum. 49 (6) (1978) 765.

[25] T. A. Shankoff, E. A. Chandross, J. Electrochem. Soc. 122 (1975) 294.

[26] F. Pobell, Matter and Methods at Low Temperatures (Springer-Verlag, Berlin Heidelberg 1992) and ref. therein.

[27] E. Gatti, P. F. Manfredi, Nuovo Cimento 9 (1986) 1.

[28] S. Cooper et al., MPI preprint MPI-PhE/93-29 (1993); A. Nucciotti et al., Proc. 3^{rd} Int. Workshop on Theoretical and Phenomenological Aspects of Underground Physics (TAUP 93), Sept. 1993, Gran Sasso Laboratory, Assergi, Italy, eds. C. Arpesella, E. Bellotti, and A. Bottino, Nucl. Phys. B (Proc. Suppl.) 35 (1994) 172.